Asymmetric Bipolar Membrane for High Current Density Electrodialysis Operation with Exceptional Stability

Éowyn Lucas[1], Justin C. Bui[2,3], Monica Hwang[1], Kaiwen Wang[1], Alexis T. Bell[3], Adam Z. Weber[4], Shane Ardo[5], Harry A. Atwater[1*], Chengxiang Xiang[1*]

[1] Division of Engineering and Applied Science, California Institute of Technology, Pasadena, CA, USA. [2] Department of Chemical and Biomolecular Engineering, University of California, Berkeley, CA, USA. [3] Chemical Sciences Division, Lawrence Berkeley National Laboratory, Berkeley, CA, USA. [4] Energy Technologies Area, Lawrence Berkeley National Laboratory, Berkeley, CA, USA. [5] Department of Chemistry, Department of Chemical & Biomolecular Engineering, and Department of Materials Science & Engineering, University of California Irvine, Irvine, CA, USA.

[*]Correspondence to haa@caltech.edu and cxx@caltech.edu

Abstract

Bipolar membranes (BPMs) enable isolated acidic/alkaline regions in electrochemical devices, facilitating optimized catalytic environments for water electrolysis, CO_2 reduction, and electrodialysis. For economic feasibility, BPMs must achieve stable, high current density operation with low overpotentials. We report a graphene oxide (GrOx) catalyzed, asymmetric BPM capable of electrodialysis at 1 A cm^{-2} with overpotentials < 250 mV. Experiments and continuum modeling demonstrate that the low overpotentials for water dissociation are achieved by deprotonation at GrOx catalyst sites located within the high electric field BPM junction region. The asymmetric nature of the BPM allows it to overcome water transport limitations due to its thin anion exchange layer, while maintaining near unity Faradaic efficiency for acid and base generation. Additionally, the asymmetric BPM exhibits voltage stability exceeding 1100 hours at 80 mA cm^{-2} and 100 hours at 500 mA cm^{-2} and its freestanding architecture implemented in an electrodialysis cell stack demonstrates its real-world applicability.

Introduction

Electrochemical technologies such as water electrolysis[1–4], CO_2 conversion[5,6], and carbon removal [6–9] are critical for making progress towards a sustainable future.[10–12] Bipolar membranes (BPMs) that demonstrate stable, high current-density operation under reverse bias have immense opportunity for implementation in such devices, due to their ability to sustain constant concentration, separated acidic and alkaline environments in a single device. The ability to sustain large differences in pH allows for cathode and anode local reaction environments that are ideal for attaining high activity, selectivity, and stability of electrocatalysts based on earth-abundant elements.[13–19] BPMs have also shown promise when integrated into salt-water fed electrodialysis cells used for pH swing-based direct air capture (DAC)[20–22] or extraction of dissolved inorganic carbon from ocean water for direct ocean capture (DOC) and ocean deacidification.[6,9,23] Stable BPM operation at high current densities (~ 1 A cm^{-2}) and low voltages (< 1.5 V) is critical to achieve low capital and operating costs in various electrochemical devices.

BPMs are comprised of a cation exchange layer (CEL) laminated to an anion exchange layer (AEL) with a water dissociation (WD) catalyst dispersed at the CEL-AEL junction.[26] At the CEL-AEL junction, mobile protons and hydroxides from the CEL and AEL react to form water, neutralizing the mobile ions to generate a space–charge depletion region of just a few nanometers, which results in a strong electric field on the order of 10^8 to 10^9 V m^{-1}.[27,28] Under reverse bias, the immense electric field present at the junction accelerates WD via the Second Wien Effect, allowing for enhanced production of H^+ and OH^-, which provide ionic currents through the CEL and AEL and enable buildup of pH gradients across the BPM.[29–32] Existing commercial BPMs (e.g.

Fumasep FBM, ASTOM BPM) are limited to stable operation at current densities up to ~100 mA cm^{-2}, as the rate of water transport through the CEL and AEL cannot match that of WD in the BPM junction at higher current densities.[26,27,33] Multiple recent efforts have attempted to overcome this water transport limitation by thinning the CEL or AEL to allow for faster water transport to the junction, successfully extending WD operating current densities to the order of 1 A cm^{-2} .[3,13,17,34]

Nonetheless, to achieve industrially relevant rates of WD with minimal applied voltage, BPMs must not only overcome water transport limitations, but also accelerate the rate of WD at the CEL-AEL junction. The addition of a catalyst at the junction further enhances the rate of WD beyond that achievable by the second Wien Effect alone. The catalyst both increases the electric field and provides an alternative path for the WD reaction per the weak acid/base model (**Section S6.3**).[26,35] A range of catalyst materials, such as polymers, metal oxides, and buffer materials have been examined experimentally for WD enhancement.[26,35,36] Previous work predicts that the concentration of ionizable sites in the CEL, AEL, and catalyst layer (CL), along with the specific pK_a values of the catalyst sites, directly affects the rate of WD at the BPM junction.[26,27,35,37,38] Neither theory nor experiments, however, have been able to determine explicitly which WD enhancement pathway dominates, leaving open a critical area for further investigation.[26,39–41]

Despite the substantial enhancements in polymer and catalyst materials for improving water transport and enhancing WD, BPMs suffer from a substantial lack of long-term stability. [26,27] In particular, very few BPMs that have been able to demonstrate high current density operation in electrodialysis, where BPMs are separated by electrolyte

channels with limited mechanical support, owing to challenges with adhesion between the two membrane bilayer elements and the CL. Recent work has sought to address this challenge by creating complex junction morphologies to improve catalytic surface area and, furthermore, increase mechanical stability.[17,34,39] However, no work has demonstrated sustained WD operation in electrodialysis for more than a few hours of uninterrupted stability at current densities >100 mA cm^{-2}.

Herein, we report a BPM comprised of a Nafion 212 CEL (~50 μm), a thin PiperION A15R AEL (~20 μm), and a graphene oxide (GrOx) WD catalyst (200 – 1000 nm) (**Figure 1**) that is stable at current densities up to 1 A cm^{-2} when tested under reverse bias in a custom-made, 5-chamber electrodialysis flow cell (**Figure S1**). GrOx was chosen as the WD catalyst because it exhibits a low WD overpotential and possesses three ionizable sites with well-defined pK_a values (**Figure 1A**). Continuum-level simulation were carried out to investigate the mechanisms of WD occurring on the GrOx layer in the BPM.[42–44] Evaluation of all contributions to the voltage of the GrOx-catalyzed, asymmetric BPM and comparison with the total experimental voltage, reveals that the BPM operates at just above the thermodynamic potential necessary for WD, with an overpotential of < 250 mV at 1 A cm^{-2}. The reported BPM is also shown to operate for over 1100 hours operation at 80 mA cm^{-2}, over 100 hours at 500 mA cm^{-2}, and over 60 hours at 1 A cm^{-2}, measured independently. This performance indicates effective water transport through the BPM and excellent stability of CEL/AEL junction. Lastly, the GrOx catalyzed, asymmetric BPM is unique in its ability to achieve similarly low overpotentials when tested freestanding in a 6 cm^{-2} salt water electrodialysis flow cell, conditions necessary for carbon capture via BPM electrodialysis (BPMED) at-scale.

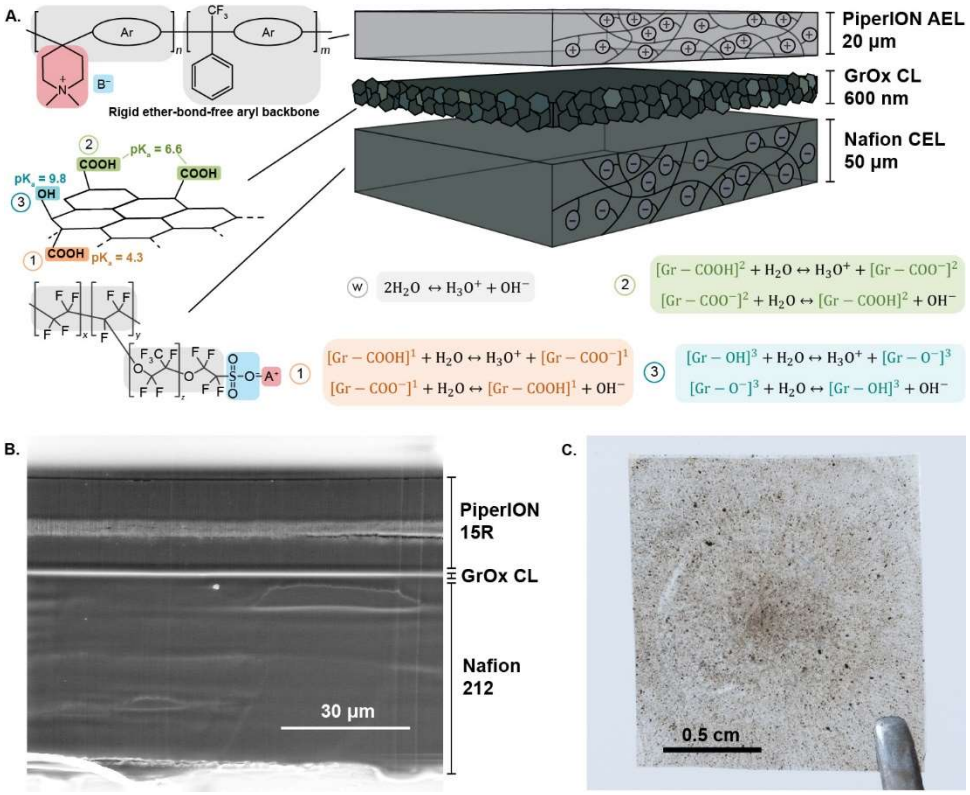

Figure 1: GrOx catalyzed, asymmetric BPM design. (A) Schematic of each layer of the BPM, indicating thickness and chemical structure. For the GrOx CL, the sites (1, 2, and 3) that contribute to WD enhancement are labeled with their pKa values and the relevant WD enhancement reactions. (B) SEM cross section of the BPM layers. The lighter region in the AEL is a mechanical support layer. (C) Picture of assembled BPM.[35,45]

Results and Discussion

Figure 1 illustrates the layers and chemical structures of the GrOx catalyzed, asymmetric BPM, along with relevant catalytic WD enhancement reactions (**Figure 1A**), a cross sectional SEM of the BPM layers (**Figure 1B**), and a picture of the fully assembled BPM (**Figure 1C**). Owing to its thin AEL and GrOx catalyst, this BPM was designed to overcome water transport limitations and enable operation at high current densities (≥500 mA cm^{-2}) typically unattainable for commercial BPMs.[46] Polarization curves for the best performing GrOx catalyzed, asymmetric BPM compared to the commercial Fumasep BPM are presented in **Figure 2A**. The ability to operate BPMs at high current densities and low voltages is desirable as it enables greater production of acid and base at lower capital and operating costs.[24,25] The GrOx catalyzed, asymmetric BPM outperformed the commercially available BPMs in all current density regions, where the performance of the Fumasep BPMs became significantly limited by either water transport or WD kinetics at current density >300 mA cm^{-2}.

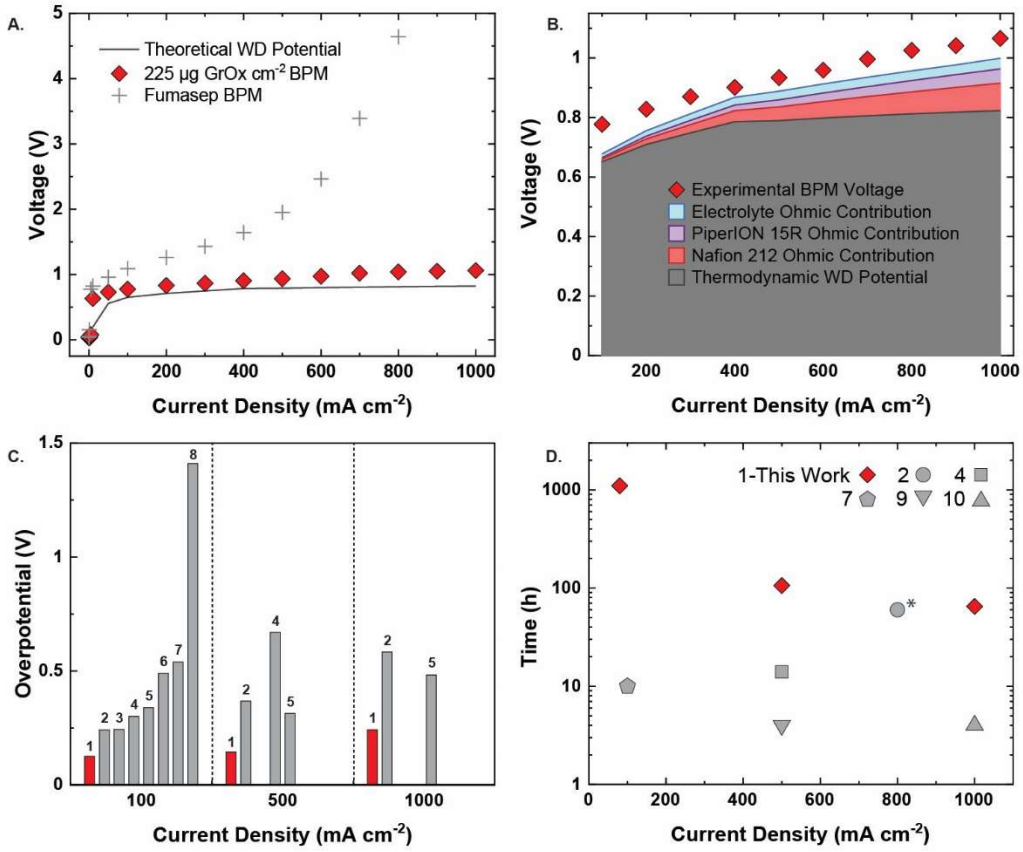

Figure 2: GrOx catalyzed, asymmetric BPM performance. (A) Polarization curves for the best performing BPM (225 μg cm^{-2} GrOx loading) and the commercial Fumasep BPM, tested in a custom electrodialysis cell, compared to the thermodynamic potential for WD. (B) Sum of voltage contributions due to WD potential, CEL ohmic losses, AEL ohmic losses, and electrolyte ohmic losses compared to measured performance of the BPM. (C) Overpotentials for the asymmetric BPM compared to other reported BPMs at 100, 500, and 1000 mA cm^{-2}. (D) Stability, in hours, at various current densities, for the reported BPM compared to other BPMs. [3,13,17,34–36,39,41,47,48] See **Table S1** for details about all compared BPMs. *Not continuous.

Figure 2B demonstrates that most of the voltage for the BPM is due to the thermodynamic potential required for WD, indicating that the BPM has been optimized for WD close to the maximum possible efficiency. Remarkably, even at a current density of 1 A cm^{-2}, the calculated kinetic overpotential is < 250 mV. The importance of the CL in obtaining these low operating overpotentials is demonstrated in **Figure S4**, in which

polarization curves of the asymmetric BPM with and without GrOx are compared. The total overpotential for high current density operation could be further reduced by making the CEL layer thinner or by increasing the ion-exchange capacity of both the CEL and AEL component. However, both changes would lead to an increase in co-ion leakage through the BPM, decreasing the efficiency for making acid and base.[38] We also note that this analysis of the BPM voltage and overpotential neglects any contributions due to pH gradients in the BPM as we are unable to measure the exact pH within the AEL and CEL; however, these contributions are expected to be minimal.[32,38]

Total overpotentials, determined as the sum of contributions due to WD kinetics, membrane resistance, and solution resistance, at 100, 500, and 1000 mA cm^{-2} were calculated for seven, top performing, BPMs.[3,13,17,34–36,39,41,47,48] Thermodynamic WD potentials at 100, 500, and 1000 mA cm^{-2} were calculated based on the testing environment described in each study (see **Section S1** for details of these calculations) and are presented in **Table S1**. The calculated total overpotentials from the seven publications were then compared to the GrOx catalyzed, asymmetric BPM in **Figure 2C**. Our BPM demonstrates the lowest overpotentials across all measured current densities, 126 mV at 100 mA cm^{-2}, 144 mV at 500 mA cm^{-2}, and 242 mV at 1 A cm^{-2}, indicating that it represents a new state-of-the-art for WD energy efficiency in BPMs. Most studies of BPMs in electrodialysis operation have not reported stability data due to problems with membrane delamination experienced by freestanding membranes when tested in saltwater environments.[26,27,47] **Figure 2D** compares the stability of the GrOx-catalyzed, asymmetric BPM with those reported for other BPMs. The points shown are the time to membrane failure, or end of reporting, at a specific current density.

Figure 3 shows voltage vs. time plots for the 3 stability points in **Figure 2D**. The asymmetric BPM exhibits excellent voltage stability at 80 mA cm^{-2} of 1100 h, at 500 mA cm^{-2} of 100 h, and at 1 A cm^{-2} of 60 h (**Figure 3**). The noise seen in the stability data is due to the formation and eventual release of dissolved gas bubbles on the surface of the BPM. Furthermore, the presence of these bubbles at the BPM surface, which only occur after > 1 hour of continuous applied current, leads to additional resistance and higher reported voltage. While many BPMs suffer from poor mechanical adhesion, commonly associated with delamination of the AEL and CEL,[26,27] the Nafion CEL and PiperION AEL used in the BPM presented in this work have excellent adhesion likely due to observed strong electrostatic interactions. Furthermore, this membrane pairing has proven to be mechanically and chemically stable under reverse bias operation as well as in acidic and basic environments.[45,49–51] The addition of a WD catalyst to the BPM junction is typically detrimental to adhesion, necessitating the use of mechanical pressure during operation.[26,27] However, the stability observed for the asymmetric BPM shows that GrOx only minimally interferes with the adhesion between Nafion and PiperION, and as fabricated, the layer-to-layer adhesion is sufficient to facilitate freestanding operation without the need for additional mechanical support.

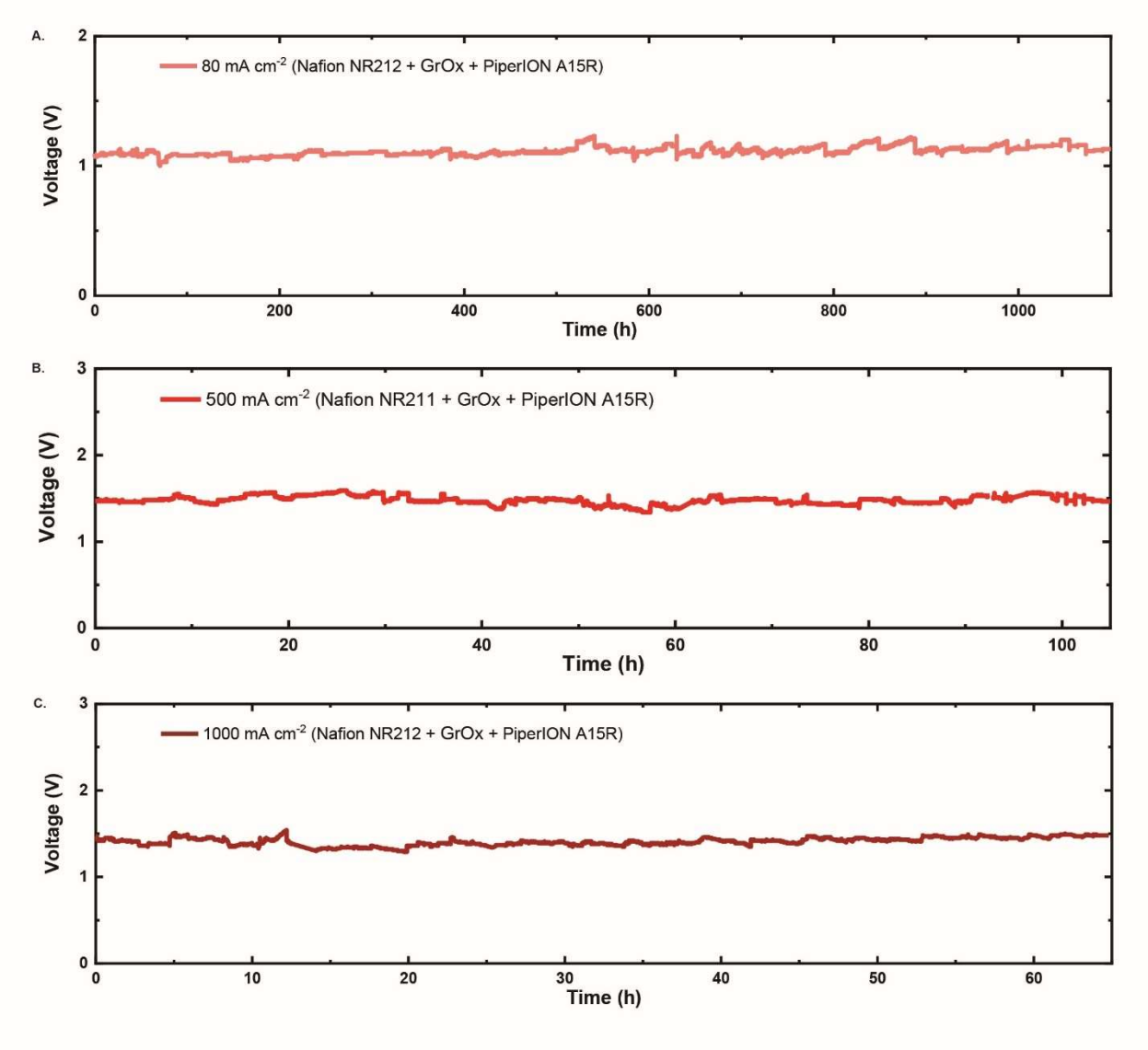

Figure 3: Voltage stability of the BPMs over time at (A) 80 mA cm^{-2}, (B) 500 mA cm^{-2}, and (C) 1000 mA cm^{-2}.

One possible hypothesis for the strong adhesion even in the presence of the GrOx CL is that the high conductivity of the GrOx enables the electrostatic forces between the AEL and CEL to maintain adhesion with minimal disruption. However, greater mechanical testing (i.e., pull tests) would be required to fully elucidate the nature of the improved adhesion when employing a GrOx-containing CL. Nonetheless, the strong layer-to-layer

adhesion of the BPM, resulting from the optimized combination of Nafion, PiperION, and GrOx, enables the BPM to overcome the stability limitations due to membrane delamination seen in many other systems.[26,27] The one stability challenge observed for the BPM was delamination due to warping of the Nafion membrane when the BPM was operated at 500 and 1000 mA cm^{-2} for multi-day stability tests. Operation at these high current densities for an extended period of time led to elevated temperatures (> 40°C) in the BPM due to the concentration of current through the custom electrodialysis cell (**Section S5**). Thus, we theorize that the elevated temperature over time cause the membranes to warp, delaminate at the junction, and eventually fail (**Section S2**).

To show that the GrOx catalyzed, asymmetric BPM is functional beyond the lab-scale (1 cm^2) diagnostic electrodialysis cell, the BPM was scaled to have an active area of 6 cm^2 (with the full size of the BPM = 35 cm^2, indicating that further scaling is possible) and tested in a thin electrodialysis cell stack (**Figure S8A and S8B**), designed to be analogous with the electrodialysis cells for acid and base generation. **Figure S8C** shows calculated voltage contributions at multiple current densities for each layer of the cell stack compared to the experimentally measured polarization curve for the BPM tested in the cell stack. The sum of the calculated voltage contributions closely matches the experimental one-cell voltage for the 6 cm^2 active area BPM across all current densities, indicating that low operating overpotentials and similar performance at high current density operation were maintained for the scaled BPM.

In addition to exhibiting scalability, low overpotentials, and exceptional stability at high current densities, the GrOx-catalyzed, asymmetric BPM exhibits excellent Faradaic efficiencies (FEs, defined as the efficiency of the applied electronic current to generate

protons and hydroxides via WD) for acid and base production at > 200 mA cm^{-2} (**Figure 4A**). Because of co-ion leakage through the thin AEL, FEs for H^+ and OH^- generation were low (~80% and lower) at operating current densities < 200 mA cm^{-2} (or < 0.8 V, **Figure 4B**). However, at current densities of > 200 mA cm^{-2} (> 0.8 V), the FEs for H^+ and OH^- generation were ~95%. This indicates that most of the current flowing through the cell goes to production of acid and base, as desired for the use of a BPM for DAC and DOC.

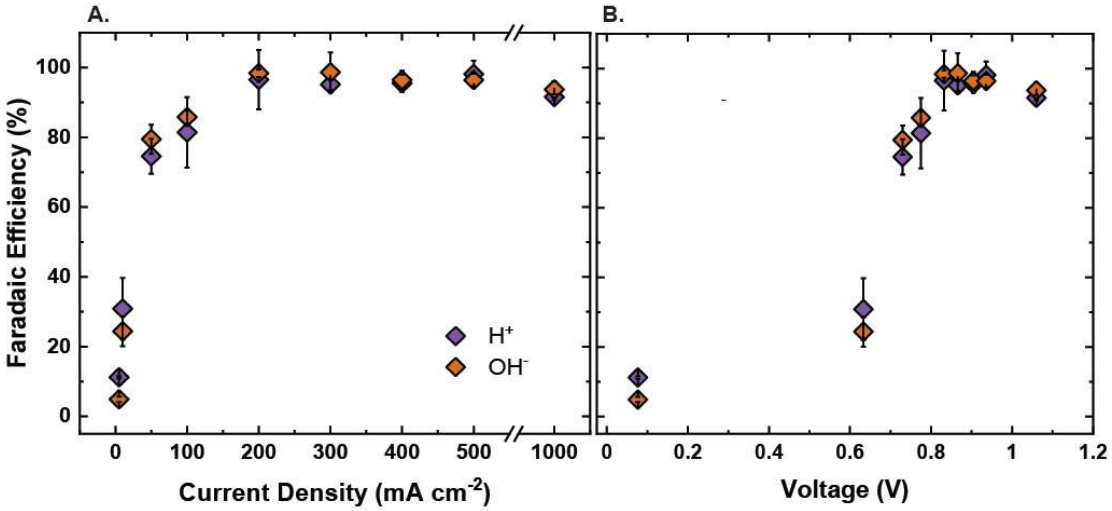

Figure 4: Faradaic efficiency for H^+ and OH^- vs. current density (A) and voltage (B) for the best performing BPM (225 µg cm^{-2} GrOx loading).

Further experiments were performed on the GrOx catalyzed, asymmetric BPMs with varied loading of GrOx ink, ranging from 75 to 325 µg cm^{-2}. The mass loading of the GrOx catalyst was varied by changing the number of layers of catalyst ink spin-coated onto the Nafion CEL during BPM fabrication. An optimal mass loading of 225 µg cm^{-2} was observed in the polarization characteristics of the GrOx catalyzed, asymmetric BPMs,

where further increasing or decreasing the mass loading lowered the BPM performance (**Figure 5**). This trend was investigated further using electrochemical impedance spectroscopy (EIS). The EIS data were fitted with a simple standard Randles circuit containing three elements (**Figure S9**): the resistance of the bulk electrolyte and bulk membranes between the two Luggin capillary tips (R_{Ω}), the resistance due to WD (R_{WD}), and the capacitance of the BPM junction (C_{WD}).[39,52] **Figure 5C** shows the relationship between the WD resistance, R_{WD}, and the GrOx catalyst loading. The R_{WD} was the lowest for the BPM at a catalyst mass loading of 225 μg cm^{-2}, exhibiting an identical trend as demonstrated by the polarization characteristics in **Figure 5A and 5B**.

The same trend was also observed for the BPM junction capacitance as a function of the GrOx catalyst loading (**Figure 5D**), where the junction capacitance was maximized at a mass loading of 225 μg cm^{-2}. As capacitance can be correlated with the number of (de)protonatable sites at the BPM junction, these data suggest a maximum number of catalytic sites for 3 layers of GrOx. Increased capacitance and activity from 1-3 layers of GrOx indicates that the catalyst coverage at the BPM junction is increasing, which is also supported by optical images and illustrations presented in **Figures 5E-5G.** The optical images and supporting diagrams, also depict that upon introduction of layers 4 and 5, GrOx noticeably aggregates, likely leading to the coverage of a percentage of the active sites available with 3 layers of GrOx.

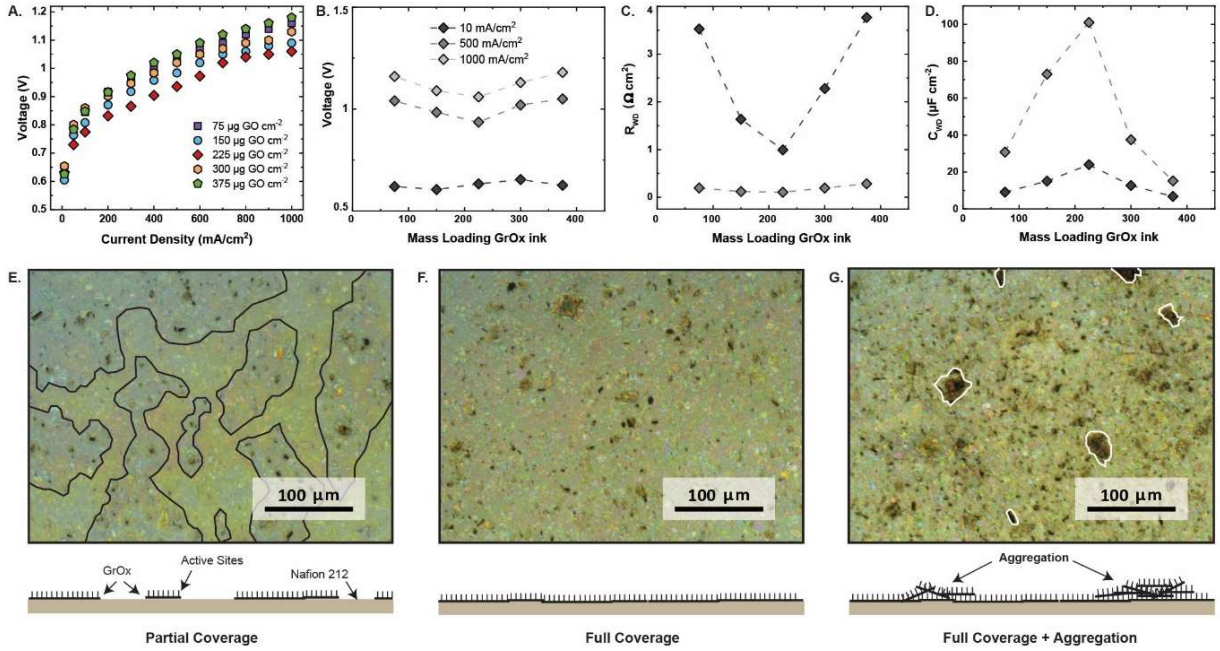

Figure 5: Effects of catalyst mass loading on WD enhancement in GrOx catalyzed, asymmetric BPM. (A) Polarization curves of BPMs with mass loading of 75-375 µg cm^{-2} of GrOx ink. Voltage (B), R_{WD} (C), and C_{WD} (D) vs. GrOx mass loading at 10, 500, and 1000 mA cm^{-2}. Optical images and supporting diagrams of (E) 1 layer of GrOx on Nafion 212, showing partial coverage of active sites (outlined in black), (F) 3 layers of GrOx on Nafion 212, showing full coverage, and (G) 5 layers of GrOx on Nafion, showing full coverage and aggregation (outlined in white).

To elucidate the mechanism of WD within the BPM, as well as the sensitivity of the BPM performance to CL properties, a continuum-level model of the BPM was developed. The model employed a continuum representation of mass conservation in which the species fluxes were defined by the Poisson–Nernst–Planck equations and homogeneous-phase bulk reactions in the BPM domain (*i.e.*, WD) were described by mass-action chemical kinetics with electric-field enhancement (**See Section S6 for model physics**). Simulation of the electric-field enhanced WD in the CL and ionic transport in the polymer and electrolyte layers reproduced the experimental polarization curves of the GrOx-catalyzed, asymmetric BPM with a high degree of accuracy (**Figure**

6A). Additionally, the model was able to accurately simulate measured salt crossover (**Figure 6A, red lines and markers**) and FEs (**Figure 6B, Figure S30**) for acid and base generation. The model also was able to define local pH and electrostatic potential profiles within the BPM and CL domains, demonstrating how the pH gradient within the BPM develops as voltage increases (**Figure S31**). Interestingly, it can be observed that most of the pH and applied potential gradient occurs at the AEL-CL interface, suggesting that WD occurs primarily at this interface.

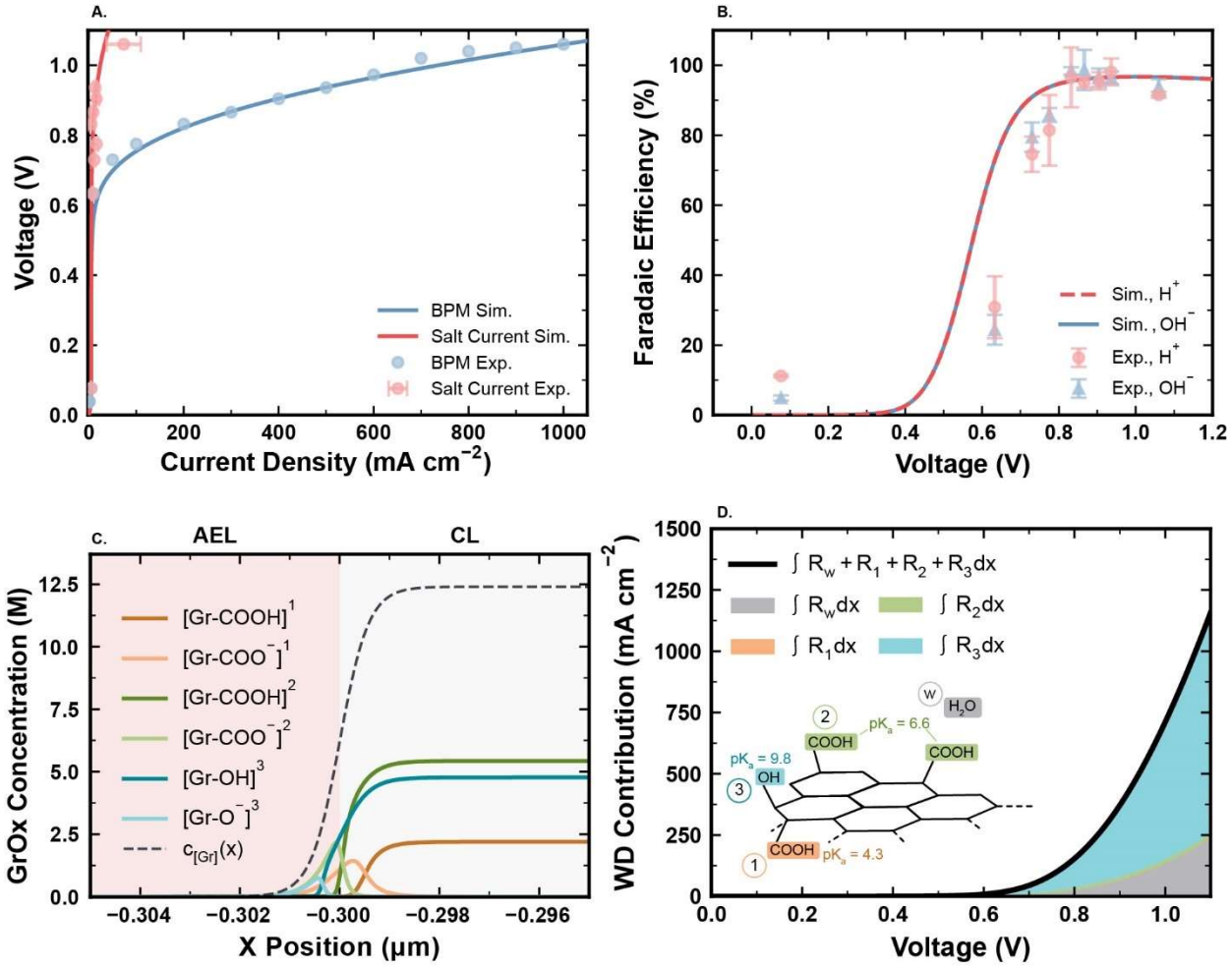

Figure 6: (A) Experimental (markers) and simulated (solid lines) polarization curves for total current density (blue) and salt-ion crossover (red). Salt crossover is calculated as described by Equation S83 in the Supporting Information. **(B)** Experimental (markers) and

simulated (lines) FE of H^+ and OH^- generation by the BPM in the catholyte and anolyte, respectively. **(C)** Concentration profiles of GrOx species at the catalytic AEL|CL interface where the bulk of WD occurs for an operating current density of 100 mA cm^{-2}. **(D)** Breakdown of WD current density due to various WD pathways **(see Figure 1A)** integrated within the BPM CL. Orange area represents contribution to WD by R_1. Green area represents contribution to WD by R_2. Blue area represents contribution to WD by R_3. Grey area represents contribution to WD by intrinsic WD pathway.

Analysis of the local electric field within the BPM CL reveals that the maximum in the electric field at the AEL-CL interface (**Figure S36-37**) coincides with the maximum the rate of WD via the Second Wien Effect (**Figure S38** and **Figure S39**). The local maximum in electric field can be explained by examining the concentration profiles of the GrOx functional groups within the CL (**Figure 6C** and **Figures S33-S35)**. Local generation of OH^- anions at the AEL-CL interface causes the most acidic GrOx functional groups (i.e., carboxylic groups) to deprotonated rapidly, resulting in a large buildup of negative charge at that interface, which, in turn, enhances the local electric field and accelerates the WD reaction via the Second Wien Effect. This finding is consistent with prior studies that suggest that the role of the catalyst is to develop surface charges that enhance the electric field and drive WD.[32,37,53] Examination of alternative WD pathways (**Equations S37-S42**, **Figure 1A**), along with experimentally determined concentrations of ionizable groups in the GrOx catalyst, shows that WD occurs primarily via the reaction of H_2O with the least acidic GrOx functional groups (i.e., phenolic groups) **(Figure 6D** and **Figure S40)**. The occurrence of WD at substantial rates by a catalyzed pathway has not been theoretically or experimentally reported before, as many prior simulations of WD observed that the uncatalyzed, but electric-field-enhanced, WD is dominant, and that the role of the catalyst is solely to assist in forming the electric field.[32,37,53] By contrast, these simulations show

that the more acidic GrOx sites serve to enhance the electric field and the least acidic GrOx sites provide additional pathways for WD. The phenolic sites are still present in > 2 M concentrations at 100 mA cm^{-2} (**Figure 6C**). Thus, the different pK_as of the acidic groups on GrOx and their high concentration within the CL (see titration in **Section S11**) are the reason that GrOx exhibits dual functionality.

To determine the extent to which the pK_a of different acidic groups in the CL affects the rate of WD, simulations of the BPM were carried out in which all sites in the CL were set to a single pK_a value equal to that of one of the pK_as associated with phenolic and carboxylic groups in GrOx (*i.e.,* either pK_a = 4.3, 6.6, or 9.8). These single-site simulations **(Figures S41-43**) were found to be consistent with those reported by Lin *et al.* who found that as the pK_a of the catalyst decreases, its WD performance improves because the acidic groups on the catalyst dissociate more readily, thereby enhancing the electric field and accelerating the rate-limiting step in WD.[37] For low pK_a (4.3 or 6.6) functional groups, WD occurs primarily via the electric-field-enhanced process, and catalyzed WD does not occur to a significant extent because of the lack of neutral sites at the AEL-CL interface (**Figure S42**).[37,53] Conversely, for higher pK_a (9.8) functional groups, catalyzed WD becomes the dominant reaction pathway, because the pK_a is sufficiently large to prevent full deprotonation. However, because there is substantially less negative charge at the AEL-CL interface in this case, the electric field, and thus the rate of WD, are significantly lower. Intriguingly, for a single pK_a = 4.3 site, the theoretical current density is much higher than for the case of multiple acidic site GrOx **(Figure S43**) due to the increase in the concentration of dissociated sites, implying that the role of the electric field enhancement is more critical to dictating WD performance. Nonetheless, the coexistence of multiple

sites on the GrOx enables the passage of WD through a catalyzed mechanism, and the multi-site GrOx CL vastly outperforms the simulated single site catalysts with $pK_a > 5$.

Continuum-level modeling also helps elucidate experimental trends observed when the mass loading of the GrOx catalyst is increased. The simulations reveal that changes in CL thickness alone cannot explain the observed trends in WD rate because WD is assumed to occur at the AEL-CL interface and not within the bulk of the CL (**Figure S44**). Further modeling demonstrates that if the volumetric concentration of catalyst sites increases concomitantly with thickness from one to three layers, the performance enhancements observed experimentally can be explained (**Figure S45**). Such an increase in the volumetric concentration of GrOx sites could result from an increase in the exposed GrOx surface with increasing CL thickness, consistent with the schematic of the GrOx structure deduced from the EIS analysis shown in **Figure 5.** While this hypothesis provides a possible explanation for the observed trends with increasing CL thickness, more detailed experimental measurements, will be required to resolve fully the effects of CL thickness on WD performance in BPMs.[54,55]

Conclusion

This study reports the successful development of a GrOx catalyzed, asymmetric BPM that overcomes water transport limitations and operates in reverse bias at high current density and low overpotentials, with high efficiencies for acid and base production. Evaluation of this BPM under conditions relevant for electrodialysis demonstrated stable operation for 1100 hours at 80 mA cm^{-2}, over 100 hours at 500 mA cm^{-2}, and over 60 hours at 1 A cm^{-2}. Additionally, at an applied current density of 1 A cm^{-2}, the BPM exhibits an overpotential of only 242 mV and a Faradaic efficiency (FE) for acid and base generation near unity. Additionally, the combination of anion exchange layer (AEL), cation exchange layer (CEL), and catalyst (PiperION, Nafion, and GrOx) chosen for the BPM enables excellent adhesion at the BPM junction, which contributes to its long-term stability. Initial testing of the BPM in an electrodialysis cell stack with a scaled active area of 6 cm^2 also demonstrated high current density operation at low voltage.

The performance of the BPM was also optimized by varying the loading of the GrOx catalyst. This effort revealed that an optimum in loading exists, whereas too low loading results in patchy coverage of the membrane interface by GrOx, which reduces the catalyst site concentration, and too high a catalyst loading results in catalyst agglomeration and a similar loss of sites. Furthermore, continuum-level modeling of the BPM closely matches the experimentally measured polarization curves and FEs. These simulations revealed that high concentrations of both low and high pK_a deprotonation sites in the GrOx CL enhance the electric field at the AEL-CL interface and provide alternative pathways for WD, enabling its exceptional performance. In summary, this work demonstrates an efficient, freestanding BPM that can be readily employed in a wide array

of electrochemical technologies in which operation with high current densities and low voltages is desirable.

Materials and Methods

Materials: Nafion 212 (50 μm, Fuel Cell Store), Nafion 211 (25 μm, Fuel Cell Store), Nafion 115 (127 μm, Fuel Cell Store), PiperION A15R (15 μm, Versogen), PiperION 20 (20 μm, Versogen), PiperION 60 (60 μm, Versogen), Fumasep FAB-PK-130 (110-140 μm, Fuel Cell Store), Fumasep FKB-PK-130 (110-140 μm, Fuel Cell Store), Nafion D520 (5 wt% Ionomer, Fuel Cell Store, IonPower), graphene oxide paste (30 g/L, Graphene Supermarket), sodium chloride (NaCl, Sigma Aldrich), sodium hydroxide (NaOH, Pellets, Macron Chemicals), hydrochloric acid (HCl, 1.0 M and 0.1 M, J. T. Baker), potassium hydroxide (KOH, pellets, Sigma-Aldrich). All membranes were received in dry form, pretreated according to manufacturer's instructions before use, and stored in DI water (CEMs) or 1 M NaOH (AEMs). All chemicals were used as received.

Catalyst ink: Catalyst inks were made by first diluting graphene oxide paste (Graphene Supermarket) from 30 g/L to 10 g/L. The dilute graphene oxide dispersion was then mixed with Nafion D520 in a 1:1 volume ratio. The final ink solution was sonicated for at least 10 minutes prior to use.

BPM fabrication: First, a piece of purchased Nafion membrane (NR212, NR211, NR115), precut into a 1.5x1.5 cm square and soaked in DI water for at least 1 h, was placed on a glass slide and patted dry with a Kim wipe. The membrane with then taped to the glass slide on all 4 sides with Kapton tape. GrOx catalyst ink was then spin coated onto the Nafion membrane at 3000 rpm for 30 s. Next, the Nafion membrane with GrOx was placed in an oven at 100°C for 2 min. This process of spin coating and heating was repeated if more layers, i.e., greater mass loading, was desired. Finally, the Nafion membrane with GrOx was rewetted with a few drops of DI water, sandwiched with the

desired thickness of PiperION membrane, and pressed firmly between gloved fingers, taking care to press out any air pockets. All membranes were tested directly after assembly. The same methods were used for fabrication of both the 1 cm^2 and 6 cm^2 active area BPMs.

Membrane conductivity measurements: The conductivity of the all AEMs and CEMs used in this work were measured using a four-point probe on a Lake Shore FastHall Station. All measurements were taken from -10 to 10 V on fully hydrated membranes. These measurements gave an in-plane conductivity, however, as the membranes are isotropic, this is equivalent to the through plane conductivity.

Measuring mass loading of GrOx: To determine the mass loading of GrOx ink spin coated onto Nafion, the Nafion membranes taped to glass slides were weighed before and after spin coating using a Sartorius CP Series electronic microbalance. Before weighing, the Nafion taped to a glass slide, was dried at 100°C for 10 min so that the measurements would not be affected by a change in hydration after the GrOx ink was added and heat treated. After the GrOx was spin coated onto the Nafion and heated, a Kim wipe was used to remove excess GrOx ink from the tape and glass. The final loading amount was calculated based on the exposed Nafion area within the tape border.

Electrodialysis cell design/assembly: Figure S1 shows a schematic of the electrodialysis cell used for testing the BPMs in this work. The cell consisted of, from left to right in schematic, an anode, an anolyte chamber, a CEM, a dilute chamber, an AEM, an acid chamber, a BPM (1 cm^2 active area), a base chamber, a CEM, a catholyte, and a cathode. Both the anode and cathode consisted of Ni foil with copper tape as leads. Aqueous 1 M NaOH with used as both the anolyte and the catholyte and was recirculated

through both chambers at ~10 mL/min. Aqueous 3 M NaCl was recirculated at ~5 mL/min through the dilute chamber and aqueous 0.5 M NaCl was flowed through the acid and base chambers at 0.2 mL/min. Both CEMs used in the cell stack were Nafion N324 (280 μm, Fuel Cell Store) and the AEM was Fumasep FAB-PK-130 (130 μm, Fuel Cell Store). Luggin capillaries holding Ag/AgCl reference electrodes (CHI111, CH Instruments) were placed in the acid and base chambers to allow for the most direct measurement of the voltage across the BPM.[18]

Chronopotentiometry: After the electrodialysis cell described above was assembled, potentiostat (Biologic SP 300, Biologic SP 200, Kiethley 2400) leads were attached in a four-point measurement configuration so that a current could be applied across the full cell and the resulting voltage could be measured directly across the BPM. Chronopotentiometry measurements were used to obtain all reported data for all polarization curves. For each point, a chosen current was applied across the anode and cathode and held steady for 5-20 min or until the voltage measured across the BPM reached steady state. The current was then increased to the next value and the process was continued until all desired current measurements were performed. The reported voltage values are averages of the voltage collected over the steady state region for each chronopotentiometry step. Examples of current density vs. time plots can be seen in **Figure S15**.

Electrochemical Impedance Spectroscopy (EIS): EIS measurements were performed in the same electrodialysis cell as the chronopotentiometry measurements. For each BPM tested, measurements were started at 500 mA cm^{-2} and stepped down through each desired current density. For each step, the current was held for 1 min, then scanned from

600 kHz to 20 Hz with an amplitude of 5-10% of the current, recording every 0.5 sec. Nyquist plots were then fitted using EIS Spectrum Analyser software (**Figure S9**).

Faradaic efficiency: The same five chamber electrodialysis cell was used for collecting acid and base samples to measure the Faradaic efficiency at various current densities. Aqueous 0.5 M NaCl was flowed at 5 mL/min through the acid and base chambers and the desired current was applied across the cell until the voltage stabilized (usually 10-20 min). Samples were then collected in 20 mL vials from the acid and base chamber. The current was then increased to the next desired value and the process repeated. Once the samples were collected, the H^+ and OH^- activity was evaluated via pH probe measurements or pH titration. Titration was used for more pH values > 12 and < 2. All pH titration measurements and the subsequent calculation of theoretical H^+/OH^- concentration and Faradaic efficiency were performed as reported in É Lucas *et al*. [18]

Low vacuum SEM: All SEM images were obtained using the low vacuum mode on an FEI Nova NanoSEM 450. A spot size of 5.0 and a voltage of 10.00 kV was used for most images. For the BPM cross-sectional images, the membrane was embedded in resin and cut using a microtome. For cross sections of just the Nafion with a GrOx CL, the membranes were sliced using a razor blade. ImageJ was used to evaluate membrane and CL thickness from these SEM cross sections.

Optical Microscopy: All optical microscope images were obtained using a Nikon Eclipse LV100D-U. Images of GrOx dispersions were taken during the BPM fabrication process, while Nafion and GrOx-coated Nafion remained taped to glass slides, before they we rewetted and sandwiched with the AEM.

AFM: An Asylum AFM in AC Air Topography mode was used for topological and roughness measurements of the membrane and GrOx layer surface. As with the optical microscope images, AFM was performed on Nafion and GrOx-coated Nafion prior to the samples being rewetted and sandwiched with the AEM.

Scaled cell stack: Figure 6A shows a schematic of the fluid flow in the electrodialysis cell used for testing the scaled BPM in this work. A commercial cell with iridium oxide-mixed metal oxide electrodes and a 6 cm^2 active area (ED 08002-010-1031-EDR, PCCell GmbH) was modified with two holes on the catholyte chamber to create inlet and outlet ports for the dilute chamber. For a single-cell stack, from anode to cathode, the membrane stack comprises of a BPM, AEM, CEM, and a BPM. All membranes were cut to a size of ~5 cm x 7 cm with a blade. 2 mm and 4 mm holes were punched in the appropriate locations to allow solution flow past the membranes for the acid and base chambers and dilute chamber, respectively. In between the membranes, a modified commercial polypropylene mesh silicone gasket (ED 08-115-085, 450 μm thickness, PCCell GmbH for the inner chambers and ED 08-115-086, 450 μm thickness, PCCell GmbH for the outer chambers) is used to allow continuous, segregated solution flow through the inner chambers (acid, base, and dilute) and outer chambers (anolyte and catholyte) of the cell. 1 M KOH solution was recirculated in two separate 5 L polypropylene reservoirs (3795T27, McMaster-Carr) for the anolyte and catholyte chambers at rate of ~1.5 L/min (BT601S-YT25, Golander Pump). 0.5 M NaCl solution flowed through the cell from separate source reservoirs for the acid, base, and dilute chambers and exited to a communal waste container at rates of ~35 mL/min (Masterflex L/S 7519-20, 2.79 mm ID

tubing, Cole-Parmer) for the acid and base channels and ~45 mL/min (PWM-controlled motor pump, 4 mm ID tubing).

Scaled cell stack chronopotentiometry: After the electrodialysis cell described above was assembled, power supply (2260-B-80-13, 360 W, Keithley) leads were attached to the cell in a two-point configuration to apply current and measure voltage. A custom LabVIEW VI controlled the applied current and chronopotentiometry measurements were used to obtain all reported current density and voltage data. For each point, a chosen current was applied across the anode and cathode and held steady for at least one minute or until the measured voltage reached steady state. Voltage data was collected at a time step of 5 s. The current was then increased to the next point and the process was continued until all desired current density measurements were obtained. The final reported voltage values are the averages of the voltage collected over a section of the steady state region for each chronopotentiometry step.

Stacked cell voltage contribution calculations: At each chosen current, under steady state, solution samples were collected in 50 mL polypropylene conical tubes from the acid, base, and dilute chambers. Once the samples were collected, the conductivity was measured using a four-ring conductivity probe (HI76312, Hanna Instruments) and meter (HI5521, Hanna Instruments). The voltage contributions for the inner chambers and ion-exchange membranes (AEM and CEM) were calculated using the following equation: $V = \frac{jL}{\sigma}$ where j is the current density (mA cm^{-2}), L is the width of the chamber (i.e., the thickness of the mesh gasket) or thickness of the membrane (cm), respectively, and K is the solution or membrane conductivity (mS cm^{-1}), respectively. The thickness of the membranes was determined using a micrometer (293-348-30, Mitutoyo). Errors in the membrane voltage

contributions were determined using the standard errors in the conductivity and thickness measurements to calculate the minimum and maximum possible voltage contributions. The average was used for the error bars in **Figure 6C**. The BPM voltage contribution was determined using this work's custom BPM testing cell as previously described.

Continuum simulation. The simulation was performed using the COMSOL Multiphysics v.6.0 software package. The concentration of H_3O^+, OH^-, Na^+, Cl^-, and of all GrOx surface species along with the electrostatic potential profile were solved using conservation equations where Poisson-Nernst-Planck described mass and charge transport. Crucially, the rates of net-charge-generating homogeneous reactions were modified by the Second Wien effect such that the rate of ion dissociation, i.e., the forward direction, was substantially enhanced by an electric field.[53,56,57] Supplementary Methods (**Section S6-S14)** provide detailed information regarding the physics and parameters employed in the simulations.

Acknowledgements

This work (materials development, fabrication, and characterization) was primarily supported as part of United States Department of Energy, Advanced Research Projects Agency–Energy (ARPA-e) under contract number DE-AR0001407 (É.L., M.H., K.W., S.A., H.A.A, C.X.). Computational work was supported by the Liquid Sunlight Alliance, which is supported by the US Department of Energy, Office of Science, Office of Basic Energy Sciences, Fuels from Sunlight Hub under award number DE-SC0021266 (J.C.B., A.T.B., A.Z.W.). J.C.B. would like to acknowledge support from the National Defense Science and Engineer Graduate Fellowship (NDSEG) supported by the Army Research Office (ARO).

Competing Interests

Two of the authors, Harry A. Atwater and CX Xiang, are stockholders of the company Captura Corporation, which has taken an option to license intellectual property from Caltech related to the bipolar membranes reported here.

Author Contributions

É.L. developed five chamber BPM testing cell, designed and fabricated BPMs, performed electrochemical experiments, characterizations, and data analysis. J.C.B. J.C.B. performed data interpretation and all continuum model calculation and figure development. M.H. Development of thin cell electrodialysis stack and testing of BPM in the stack. K.W. temperature environment simulations and figure development. A.T.B., A.Z.W., S.A., H.A.A., and C.X. supervised the project. All authors discussed results and participated in the preparation of the manuscript.

References

1. Thiele, S. *et al.* Bipolar membrane electrode assemblies for water electrolysis. *ACS Appl Energy Mater* **3**, 9635–9644 (2020).

2. Ge, Z. *et al.* High-performance bipolar membrane for electrochemical water electrolysis. *J Memb Sci* **656**, (2022).

3. Thiele, S. *et al.* On the effect of anion exchange ionomer binders in bipolar electrode membrane interface water electrolysis. **9**, 14105–14610.

4. Wang, X. *et al.* Balancing Water Dissociation and Current Densities to Enable Sustainable Hydrogen Production with Bipolar Membranes in Microbial Electrolysis Cells. *Environ. Sci. Technol* **53**, 14761–14768 (2019).

5. Zhou, X. *et al.* Solar-Driven Reduction of 1 atm of CO_2 to Formate at 10% Energy-Conversion Efficiency by Use of a TiO_2-Protected III-V Tandem Photoanode in Conjunction with a Bipolar Membrane and a Pd/C Cathode. *ACS Energy Lett* **1**, 764–770 (2016).

6. Digdaya, I. A. *et al.* A direct coupled electrochemical system for capture and conversion of CO_2 from oceanwater. *Nat Commun* **11**, 1–10 (2020).

7. Xu, J. *et al.* Review on electrochemical carbon dioxide capture and transformation with bipolar membranes. *Chinese Chemical Letters* 108075 (2022) Doi: 10.1016/j.cclet.2022.108075.

8. Jin, S., Wu, M., Jing, Y., Gordon, R. G. & Aziz, M. J. Low energy carbon capture via electrochemically induced pH swing with electrochemical rebalancing. doi:10.1038/s41467-022-29791-7.

9. Liu, Y., Lucas, É., Sullivan, I., Li, X. & Xiang, C. Challenges and opportunities in continuous flow processes for electrochemically mediated carbon capture. *iScience* **25**, 105153 (2022).

10. Climate Change 2022: Mitigation of Climate Change. https://www.ipcc.ch/report/ar6/wg3/?itid=lk_inline_enhanced-template.

11. McKay, D. I. A. *et al.* Exceeding 1.5°C global warming could trigger multiple climate tipping points. *Science (1979)* **377**, (2022).

12. Rogelj, J. *et al.* Scenarios towards limiting global mean temperature increase below 1.5°C. *Nature Climate Change 2018 8:4* **8**, 325–332 (2018).

13. Oener, S. Z., Twight, L. P., Lindquist, G. A. & Boettcher, S. W. Thin Cation-Exchange Layers Enable High-Current-Density Bipolar Membrane Electrolyzers via Improved Water Transport. *ACS Energy Lett* **6**, 1–8 (2021).

14. Vermaas, D. A., Wiegman, S., Nagaki, T. & Smith, W. A. Ion transport mechanisms in bipolar membranes for (photo)electrochemical water splitting. *Sustain Energy Fuels* **2**, 2006–2015 (2018).

15. Sun, K. *et al.* A Stabilized, Intrinsically Safe, 10% Efficient, Solar-Driven Water-Splitting Cell Incorporating Earth-Abundant Electrocatalysts with Steady-State pH Gradients and Product Separation Enabled by a Bipolar Membrane. *Adv Energy Mater* **6**, 1600379 (2016).

16. Vargas-Barbosa, N. M. *et al.* Assessing the Utility of Bipolar Membranes for use in Photoelectrochemical Water-Splitting Cells. *ChemSusChem* **7**, 3017–3020 (2014).

17. Powers, D. *et al.* Freestanding Bipolar Membranes with an Electrospun Junction for High Current Density Water Splitting. *Cite This: ACS Appl. Mater. Interfaces* **14**, 36092–36104 (2022).

18. Lucas, É., Han, L., Sullivan, I., Atwater, H. A. & Xiang, C. Measurement of ion transport properties in ion exchange membranes for photoelectrochemical water splitting. *Front Energy Res* **10**, 1383 (2022).

19. McDonald, M. B., Bruce, J. P., McEleney, K. & Freund, M. S. Reduced Graphene Oxide Bipolar Membranes for Integrated Solar Water Splitting in Optimal pH. *ChemSusChem* **8**, 2645–2654 (2015).

20. Erans, M. *et al.* Direct air capture: process technology, techno-economic and socio-political challenges. *This journal is Cite this: Energy Environ. Sci* **15**, 1360 (2022).

21. Ozkan, M., Nayak, S. P., Ruiz, A. D. & Jiang, W. Current status and pillars of direct air capture technologies. *iScience* **25**, (2022).

22. Fasihi, M., Efimova, O. & Breyer, C. Techno-economic assessment of CO_2 direct air capture plants. *J Clean Prod* **224**, 957–980 (2019).

23. Jayarathna, C., Maelum, M., Karunarathne, S., Andrenacci, S. & Haugen, H. A. Review on direct ocean capture (DOC) technologies. (2022).

24. Sabatino, F., Gazzani, M., Gallucci, F. & van Sint Annaland, M. Modeling, Optimization, and Techno-Economic Analysis of Bipolar Membrane Electrodialysis for Direct Air Capture Processes. *Ind Eng Chem Res* **61**, 12668–12679 (2022).

25. Sabatino, F. *et al.* Evaluation of a Direct Air Capture Process Combining Wet Scrubbing and Bipolar Membrane Electrodialysis. (2020) Doi: 10.1021/acs.iecr.9b05641.

26. Pärnamäe, R. *et al.* Bipolar membranes: A review on principles, latest developments, and applications. *J Memb Sci* **617**, 1–25 (2021).

27. Giesbrecht, P. K. & Freund, M. S. Recent Advances in Bipolar Membrane Design and Applications. *Chemistry of Materials* **32**, 8060–8090 (2020).

28. Schulte, L., White, W., Renna, L. A. & Ardo, S. Turning water into a protonic diode and solar cell via doping and dye sensitization. *Joule* **5**, 2380–2394 (2021).

29. Mafé, S., Ramírez, P. & Alcaraz, A. Electric field-assisted proton transfer and water dissociation at the junction of a fixed-charge bipolar membrane. *Chem Phys Lett* **294**, 406–412 (1998).

30. Alcaraz, A., Ramírez, P., Mafé, S., Holdik, H. & Bauer, B. Ion selectivity and water dissociation in polymer bipolar membranes studied by membrane potential and current-voltage measurements. *Polymer (Guildf)* **41**, 6627–6634 (2000).

31. Strathmann, H., Krol, J. J., Rapp, H. J. & Eigenberger, G. Limiting current density and water dissociation in bipolar membranes. *J Memb Sci* **125**, 123–142 (1997).

32. Bui, J. C., Corpus, K. R. M., Bell, A. T. & Weber, A. Z. On the Nature of Field-Enhanced Water Dissociation in Bipolar Membranes. *Journal of Physical Chemistry C* **125**, 24974–24987 (2021).

33. Aritomi, T., van den Boomgaard, T. & Strathmann, H. Current-voltage curve of a bipolar membrane at high current density. *Desalination* **104**, 13–18 (1996).

34. Shen, C., Wycisk, R. & Pintauro, P. N. High performance electrospun bipolar membrane with a 3D junction. *Energy Environ Sci* **10**, 1435–1442 (2017).

35. Oener, S. Z., Foster, M. J. & Boettcher, S. W. Accelerating water dissociation in bipolar membranes and for electrocatalysis. *Science (1979)* **369**, 1099–1103 (2020).

36. Hohenadel, A. *et al.* Electrochemical Characterization of Hydrocarbon Bipolar Membranes with Varying Junction Morphology. *ACS Appl Energy Mater* **2**, 6817–6824 (2019).

37. Lin, M., Digdaya, I. A. & Xiang, C. Modeling the electrochemical behavior and interfacial junction profiles of bipolar membranes at solar flux relevant operating current densities. *Sustain Energy Fuels* **5**, 2149–2158 (2021).

38. Bui, J. C., Digdaya, I., Xiang, C., Bell, A. T. & Weber, A. Z. Understanding Multi-Ion Transport Mechanisms in Bipolar Membranes. *ACS Appl Mater Interfaces* **12**, 52509–52526 (2020).

39. Al-Dhubhani, E. *et al.* Entanglement-Enhanced Water Dissociation in Bipolar Membranes with 3D Electrospun Junction and Polymeric Catalyst. *ACS Appl Energy Mater* **4**, 3724–3736 (2021).

40. Hohenadel, A., Gangrade, A. S. & Holdcroft, S. Spectroelectrochemical Detection of Water Dissociation in Bipolar Membranes. *ACS Appl Mater Interfaces* **13**, 46125–46133 (2021).

41. Yan, Z. *et al.* The balance of electric field and interfacial catalysis in promoting water dissociation in bipolar membranes †. *Energy Environ. Sci* **11**, 2235 (2018).

42. Konkena, B. & Vasudevan, S. Understanding Aqueous Dispersibility of Graphene Oxide and Reduced Graphene Oxide through pKa Measurements. *J. Phys. Chem. Lett* **3**, 872 (2012).

43. Orth, E. S. *et al.* PKa determination of graphene-like materials: Validating chemical functionalization. *J Colloid Interface Sci* **467**, 239–244 (2016).

44. Publication Classification (54) MEMBRANES FOR ENHANCING RATES OF WATER DISSOCIATION AND WATER FORMATION (71) Applicant: THE REGENTS OF THE. (2021).

45. Wang, J. *et al.* Poly(aryl piperidinium) membranes and ionomers for hydroxide exchange membrane fuel cells. *Nat Energy* **4**, 392–398 (2019).

46. Blommaert, M. A. *et al.* Insights and Challenges for Applying Bipolar Membranes in Advanced Electrochemical Energy Systems. *ACS Energy Lett* **6**, 2539–2548 (2021).

47. Chen, Y. *et al.* High-Performance Bipolar Membrane Development for Improved Water Dissociation. *ACS Appl Polym Mater* (2020) doi:10.1021/acsapm.0c00653.

48. McDonald, M. B. & Freund, M. S. Graphene oxide as a water dissociation catalyst in the bipolar membrane interfacial layer. *ACS Appl Mater Interfaces* **6**, 13790–13797 (2014).

49. Luo, X., Rojas-Carbonell, S., Yan, Y. & Kusoglu, A. Structure-transport relationships of poly(aryl piperidinium) anion-exchange membranes: Effect of anions and hydration. *J Memb Sci* **598**, 117680 (2020).

50. Thuc, V. D., Cong Tinh, V. D. & Kim, D. Simultaneous improvement of proton conductivity and chemical stability of Nafion membranes via embedment of surface-modified ceria nanoparticles in membrane surface. *J Memb Sci* **642**, 119990 (2022).

51. Zhou, Y. *et al.* Rational use and reuse of Nafion 212 membrane in vanadium flow batteries. *RSC Adv* **7**, 19425–19433 (2017).

52. Blommaert, M. A., Vermaas, D. A., Izelaar, B., In'T Veen, B. & Smith, W. A. Electrochemical impedance spectroscopy as a performance indicator of water dissociation in bipolar membranes. *J Mater Chem A Mater* **7**, 19060–19069 (2019).

53. Craig, N. P. Electrochemical Behavior of Bipolar Membranes. (2013).

54. Zenyuk, I. V, Das, P. K. & Weber, A. Z. Understanding Impacts of Catalyst-Layer Thickness on Fuel-Cell Performance via Mathematical Modeling. *J Electrochem Soc* **163**, F691–F703 (2016).

55. Bui, J. C. *et al.* Continuum modeling of porous electrodes for electrochemical synthesis. *Chem Rev* **122**, 11022–11084 (2022).

56. Onsager, L. Deviations from Ohm's Law in Weak. *J. Chem. Phys.* **2**, 599–615 (1934).

57. Kaiser, V., Bramwell, S. T., Holdsworth, P. C. W. & Moessner, R. Onsager's Wien Effect on a Lattice. *Nat. Mater.* **12**, 1033–1037 (2013).